MATERIALS SCIENCE

# Study of self-assembly behavior and ionic conductivity of conjugated liquid crystals with T-shaped facial-polyphilic structure

**Ziwei Liu[1]†, Yangyang Sun[2]†, Ban Xuan Dong[3,4]†, Shrayesh N. Patel[4,5], Paul F. Nealey[4,5]*, Fernando A. Escobedo[2]*, Christopher K. Ober[1]***



**The unique self-assembly of liquid crystals (LCs), combined with their potential application as organic semiconductors, has become a focus of recent research. Here, a joint experimental and computational study of the self-assembly and ionic conduction was carried out on a series of T-shaped conjugated LCs consisting of three incompatible components. By extending the EOn side-chain length, several experimental evaluations confirmed a decrease of the order-disorder transition temperature, while coarse-grained simulations revealed a structural evolution from a smectic phase to a columnar phase. Ionic conductivity of these molecules was achieved by adding Li salt, leading to a maximum conductivity of $1.1 \times 10^{-3}$ siemens per centimeter observed at 120°C. All-atom simulations were performed to examine the Li-ion solvation environment and to evaluate the intrachain and interchain Li-ion hopping mechanisms. The molecule with a long EOn side chain was found to generate a densely distributed network of Li-ion solvation sites, which can facilitate effective interchain hopping to promote ion transport.**

## INTRODUCTION

Conjugated liquid crystals (LCs) have attracted broad interest in the field of organic semiconductors due to their tunable processibility and mechanical flexibility compared to their inorganic counterparts (*1*–*5*), leading to diverse applications in solar cells (*6*–*9*), light-emitting diodes (*10*–*13*), and field effect transistors (*14*–*16*). The unique feature of LC states combining overall structural order and individual molecular fluidity enables molecules to align uniformly over a large area with no grain boundaries (*14*, *17*, *18*), to self-heal local packing defects (*3*), and to respond to external stimuli, such as mechanical force, heat, light, and so on (*19*–*22*). Unlike intrinsic molecular properties, the transport of charge carriers in organic semiconductors mainly depends on their molecular packing (*5*, *23*), and the self-assembly of LC molecules is driven by the nanoscale segregation of immiscible constituent segments. In a typical conjugated LC molecule, rigid rod-like (calamitic) or disk-like (discotic) π-conjugated moieties can provide necessary shape anisotropy to better align the molecule for the electron or hole transport, and nonconducting alkyl groups can provide some flexibility to facilitate the molecular assembly and to form insulating domains to alter the shape of charge transport channels (*2*, *23*). Recently, there has been a growing interest in developing LC conductors that can transport electrons and ions simultaneously by attaching ionic or polar groups to π-conjugated moieties (*24*–*28*). Among different ion-conducting chemistries, poly(ethylene oxide) (PEO) has garnered most attention due to its excellent solvating affinity with alkali metal cations, improved thermal stability, reduced flammability, and facile processibility (*29*–*31*).

To improve the performance of organic semiconductors, extensive experimental efforts have been made to synthesize LC molecules forming differently shaped transport pathways for charge carriers including lamellae (*32*–*34*), columns (*2*, *35*, *36*), and networks (*37*, *38*). Given the molecular design versatility in organic chemistry, a rational design strategy is desirable to construct intricate LC structures by tailoring the molecular shape anisotropy and selecting proper functional groups to tune intermolecular interactions (*23*, *39*, *40*). Molecular dynamic (MD) simulations can serve as a complementary approach to time-consuming experimental synthesis and characterization, to rapidly explore the self-assembly behavior of candidate LC molecules (*41*, *42*). For electron transport, MD simulations can facilitate the structure determination of a material to extract important packing details like the molecular orientation and π-π stacking (*27*, *28*). Numerous theoretical and computational studies have shown that the cation transport in PEO is intrinsically related to the segmental motion through three principal mechanisms including intrachain hopping along a polymer chain, interchain hopping, and codiffusion with short polymer chains (*31*, *43*). However, it remains unclear to what extent the knowledge gathered from well-studied bulk PEO-based systems can be applied to conjugated LC systems with dispersed, nanoscale-thick ion-conducting domains. MD simulations can provide mechanistic insights by directly examining the ion solvation environment and evaluating the relative motions between ions and LCs.

Our previous studies showed that linear amphiphilic LC molecules containing a rigid oligothiophene core attached with flexible oligo(ethylene oxide) (EOn) segments at both ends only form the smectic phase (*26*, *28*). To increase the self-assembled structural complexity and the resulting phase diversity, previous experimental studies have resorted to incorporating multiple immiscible segments and modifying the molecular shape (*39*, *40*). In this work, we combine experimental and computational efforts to investigate the self-assembly and the charge conduction in a series of T-shaped

[1]Department of Materials Science and Engineering, Cornell University, Ithaca, NY 14853, USA. [2]Smith School of Chemical and Biomolecular Engineering, Cornell University, Ithaca, NY 14853, USA. [3]Advanced Materials and Applications Research Group (AMA-HUTECH), HUTECH University, 475A Dien Bien Phu Street, Binh Thanh District, Ho Chi Minh City, 700000, Vietnam. [4]Pritzker School of Molecular Engineering, The University of Chicago, Chicago, IL 60637, USA. [5]Materials Science Division, Argonne National Laboratory, Lemont, IL 60439, USA.
*Corresponding author. Email: cko3@cornell.edu (C.K.O.); nealey@uchicago.edu (P.F.N.); fe13@cornell.edu (F.A.E.)
†These authors contributed equally to this work.

facial polyphilic LC molecules that engender higher phase complexity. This is done by attaching hexyl groups at both ends of a rigid pentathiophene (5T) core (forming the molecular backbone) and an EOn segment on the central thiophene as a flexible side chain; the resulting T-shaped molecules will be denoted 5T/di-hexyl/EOn or 5T/dC6/EOn for simplicity. Compared to conventional linear LCs, T-shaped variants exhibit a distinctive molecular architecture that enables intriguing properties through enhanced molecular anisotropy and packing flexibility (*40*). Thermal properties of these compounds were examined, showing a decreased mesophase transition temperature for the molecule with a longer EOn side chain. MD simulations and wide-angle x-ray scattering (WAXS) were performed to reveal the structure evolution of 5T/dC6/EOn, which varied with EOn segmental length from a smectic phase with complex in-plane packing to a columnar phase. The ion transport in 5T/dC6/EOn was measured in the presence of the ionic dopant, lithium bis(trifluoromethanesulfonyl)imide (LiTFSI), at a doping ratio defined as the molar fraction between Li-ions and EO units, $r = [Li^+]/[EO]$. The ionic conductivity of 5T/dC6/EOn was found to increase with the EOn segmental length at a LiTFSI doping ratio of $r = 0.05$, while the electronic conductivity was disrupted by the EOn clusters and is not discussed here. In addition, the Li-ion solvation environment in the ion-conducting domains was characterized by MD simulations to provide a more detailed characterization of the Li-ion transport mechanism.

## RESULTS

### Synthesis of 5T/dC6/EOn

T-shaped polyphilic LC molecules, 5T/dC6/EOn, were synthesized by twofold Suzuki coupling reaction using $Pd(PPh_3)_4$ as catalyst, as illustrated in fig. S1 of the Supplementary Materials. Subject to our purchased reagents, the chemical formula of 5T/dC6/EO3 and 5T/dC6/EO4 refers to the exact number of EO units in each molecule, while 5T/dC6/EO10 is an estimated formula, since 5T/dC6/EO10 was synthesized using a mixture of EOn chains with the average number of EO units per chain being $n = 10$. The polydisperse EOn side chains in the synthesized 5T/dEO6/EO10 system play a limited role in the assembled structure as confirmed by our preliminary simulations, where similar columnar phases were formed by different monodisperse 5T/dC6/EOn systems ranging from $n = 8$ to $n = 12$. Also related to reagents, 5T/dC6/EO4 and 5T/dC6/EO10 contain an extra carbon spacer between the 5T core and the EOn side chain. The compounds of 5T/dC6/EO3 and 5T/dC6/EO4 are yellow powders at room temperature, while 5T/dC6/EO10 remains dark red liquid. All products are characterized by $^1H$ and $^{13}C$ nuclear magnetic resonance (NMR) spectroscopy. Detailed synthetic procedures are shown in section S1.2.

### Thermal properties of 5T/dC6/EOn

For 5T/dC6/EOn compounds, their thermal properties were characterized by differential scanning calorimetry (DSC), and their optical textures exhibiting LC phases were obtained by polarized optical microscopy (POM) at room temperature. DSC traces in Fig. 1A show the first cooling scan and the second heating scan obtained for all samples in their pristine states with transition temperatures and transition enthalpies listed next to the transition peaks. Here, given the polydisperse nature of 5T/dC6/EO10, we use joules per gram as the unit of the transition enthalpy. More detailed information is displayed in table S1. The thermal decomposition temperatures of selected 5T/dC6/EOn are shown in fig. S2. Both samples of 5T/dC6/EO3 and 5T/dC6/EO4 exhibit stable LC mesophases at room temperature. 5T/dC6/EO3 shows a clear exothermic phase transition at 31°C in the cooling process and an endothermic phase transition at 48°C in the heating process. 5T/dC6/EO4 with one more EO unit shows a phase transition at a lower temperature (20°C during cooling and 35°C during heating). 5T/dC6/EO10 with a relatively long EOn side chain does not show any LC mesophase around room temperature, and its phase transition takes place at −36°C during cooling process and at 4°C during heating process with broader peaks likely related to nonuniform EOn side chains. We notice that extending the EOn side chain from $n = 3$ to $n = 10$ reduces the order-disorder transition temperature of 5T/dC6/EOn between the LC state and isotropic state of each molecule. As we have discussed in our previous work (*44*) on linear structured LC 4T/PEOn, in nanosegregated two-domain LC in which one domain is highly ordered (thiophene) and the other domain is less ordered and liquid-like (PEO), the length of PEO chains determines the material's melting behavior. With the increasing length of PEO chains, the associated increase in conformational entropy drives a tendency toward disorder that overtakes the cohesive energy, keeping the ordered

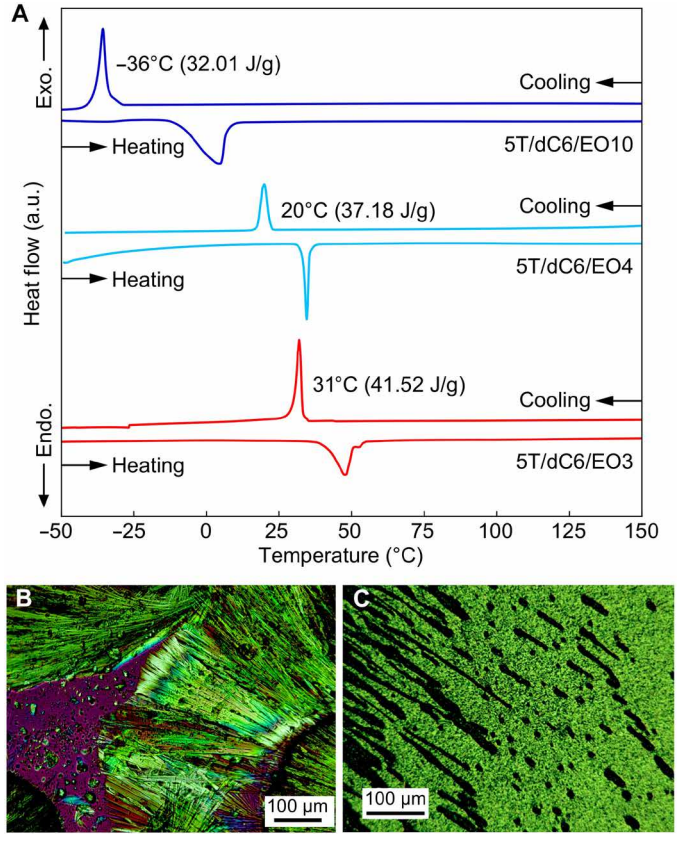


**Fig. 1. Thermal and optical properties of 5T/dC6/EOn.** (**A**) DSC traces of pristine states of 5T/dC6/EOn measured at a scanning rate of 10°C/min. For each product, the top trend is the first cooling cycle, and the bottom trend is the second heating cycle. Order-disorder transition temperatures are listed near transition peaks for each molecule with transition enthalpies in parenthesis. (**B**) POM images measured in the pristine bulk phase at room temperature of 5T/dC6/EO3 and (**C**) 5T/dC6/EO4. Scale bars, 100 μm. a.u., arbitrary units.

packing of the 4T domains. A similar theory can also be applied to the three-component system 5T/dC6/EOn, where conjugated oligothiophene forms the rigid skeleton and EOn segments introduce flexibility to the system. Therefore, increasing the length of EOn segments consequently leads to decreased phase transition temperatures. The transition enthalpy of each molecule follows the same monotonic decreasing trend as the length of EOn segments increases and the molecule becomes more flexible and mobile, which renders the LC structure less stable. In summary, extending the EOn side chain reduces the transition temperature and enthalpy of 5T/dC6/EOn between LC and isotropic states.

Following the same method in our previous work (*26*), POM images were taken at 20°C for the bulk materials of LC compounds except for 5T/dC6/EO10, since its order-disorder phase transition takes place below room temperature. In addition to the birefringent batonnet textures usually found in traditional LC structures (Fig. 1, B and C), more crystalline features, such as the needle-shaped character, were detected for 5T/dC6/EO3 due to potential local crystallinity of EOn side chains and 5T-conjugated moieties (Fig. 1B). This material is therefore believed to be highly ordered LCs (*45*) or defect-rich "condis" crystals (*46*) in which the loss/lack of positional mobility can be attributed to short flexible spacer length and low-efficiency packing of alkyl chains.

## Molecular packing of 5T/dC6/EOn

The self-assembly of 5T/dC6/EOn molecules was simulated using the coarse-grained (CG) model (Fig. 2A and figs. S3 and S4) through a regular quenching process, where ordered structures were formed at lower temperatures (see fig. S5 in section S3). For 5T/dC6/EO3 and 5T/dC6/EO4 with a shorter EOn side chain, a lamella phase with complex in-layer packing self-assembled, where alkyl segments form one layer and the 5T and EOn segments together form another adjacent layer (Fig. 2B). Moreover, in the latter two-component layer, EOn segments are grouped into small clusters interspersed within the well-aligned stacks of 5T segments. As for 5T/dC6/EO10 which has a longer EOn side chain, a columnar phase was self-assembled, where the more rigid molecular backbones (5T with alkyl groups) form a continuous domain to delineate the shell of each cylinder while the EO10 segments aggregate into many isolated domains that fill the space inside each cylinder (Fig. 2C).

Since well-aligned 5T segments are often found in CG configurations, it is of interest to further examine the packing structure of thiophene rings in a model vested with the necessary atomistic details. Thus, a representative atomistic configuration of 5T/dC6/EO3 was initially generated from its CG self-assembled structure and then thermally equilibrated using the all-atom (AA) force field. The calculated diffraction pattern is an effective representation to examine the periodic order embedded in the AA configuration. The grazing incidence wide-angle x-ray scattering (GIWAXS) pattern was adopted for a convenient comparison with the experimental results measured in the thin films of 5T/dC6/EOn. A detailed analysis of this framework has been well-documented in our previous study (*28*). Usually, the GIWAXS pattern is plotted over the space spanned by $\boldsymbol{q}_r$ and $\boldsymbol{q}_z$ to reveal structural information in the direction parallel (in-plane, radially along $r$) and perpendicular (out-of-plane, along the $z$ axis) to the film, respectively.

In the simulations, a diffraction pattern is calculated by setting the lamella stacking direction in an AA configuration as the out-of-plane $z$ direction (Fig. 3A), which is consistent with the experimental

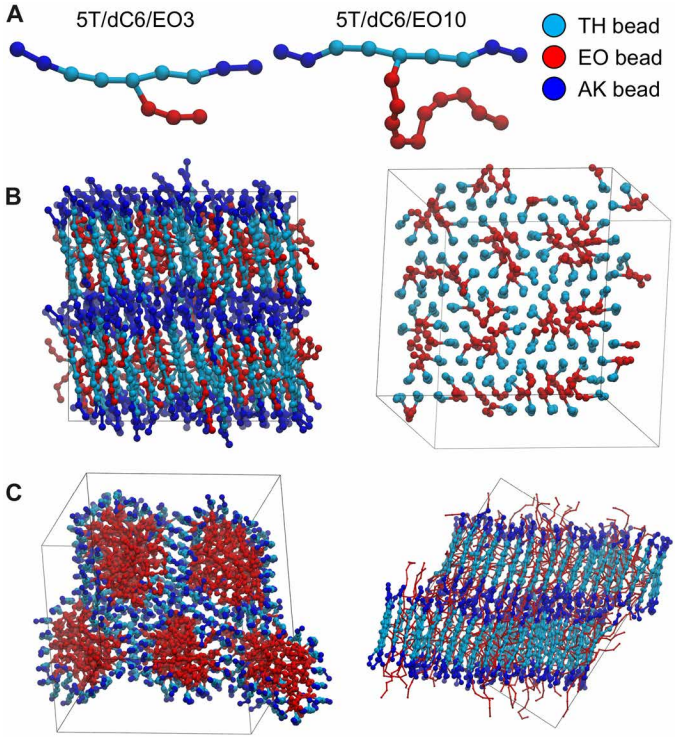


**Fig. 2. Self-assembly of 5T/dC6/EOn in simulations.** (**A**) CG model of a single molecule. A TH bead represents a thiophene ring, an EO bead represents one ethylene oxide unit, and an AK bead represents a propyl alkyl group. (**B**) 5T/dC6/EO3 forming lamellar phase from the out-of-plane (left) and in-plane (right) directions. For clarity, only a two-component layer with 5T and EO3 is shown in the right snapshot. (**C**) 5T/dC6/EO10 forming columnar phase from a cross-sectional (left) and longitudinal (right) directions. EO10 segments in the right snapshot are drawn with thinner lines to more clearly show the alignment of 5T segments.

setup. Several relationships can be established between peaks in a diffraction pattern and packing features in an AA configuration using Miller indices (integers $h$, $k$, and $l$), which define a set of parallel planes with equal interplanar spacing to represent different periodic types. Here, the in-plane Miller indices refer to $h$ and $k$, the out-of-plane index refers to $l$, and negative integers are written with an underbar. For the simulated pattern shown in Fig. 3A, peaks along the edge of $q_r \approx 0$ are related to the formation of a lamellar structure. The peak with an intermediate intensity at $q_r \approx 0.34$ Å$^{-1}$ reveals that those isolated EOn clusters are arranged in a certain periodic manner. Strong peaks between $q_r \approx 1.32$ Å$^{-1}$ and $q_r \approx 1.39$ Å$^{-1}$ pertain to the packing structure of 5T segments, which can be labeled with in-plane Miller indices of {1$\underline{1}$ L}, {20 L}, and {11 L} to confirm a two-dimensional centered lattice within a lamella (fig. S6). {1$\underline{1}$ L} and {11 L} peaks with different $q_r$ values indicate a parallelogrammatic unit cell rather than a rectangular one (*28*), which can be attributed to the disruption and deformation of the regular packing of 5T segments by EOn clusters. Also, 5T segments from different layers aligning in the same direction contribute to the strong peak intensities.

In the experiments, GIWAXS patterns were measured at room temperature only for the thin film of 5T/dC6/EO3 and 5T/dC6/EO4 due to the much lower order-disorder transition temperature of 5T/

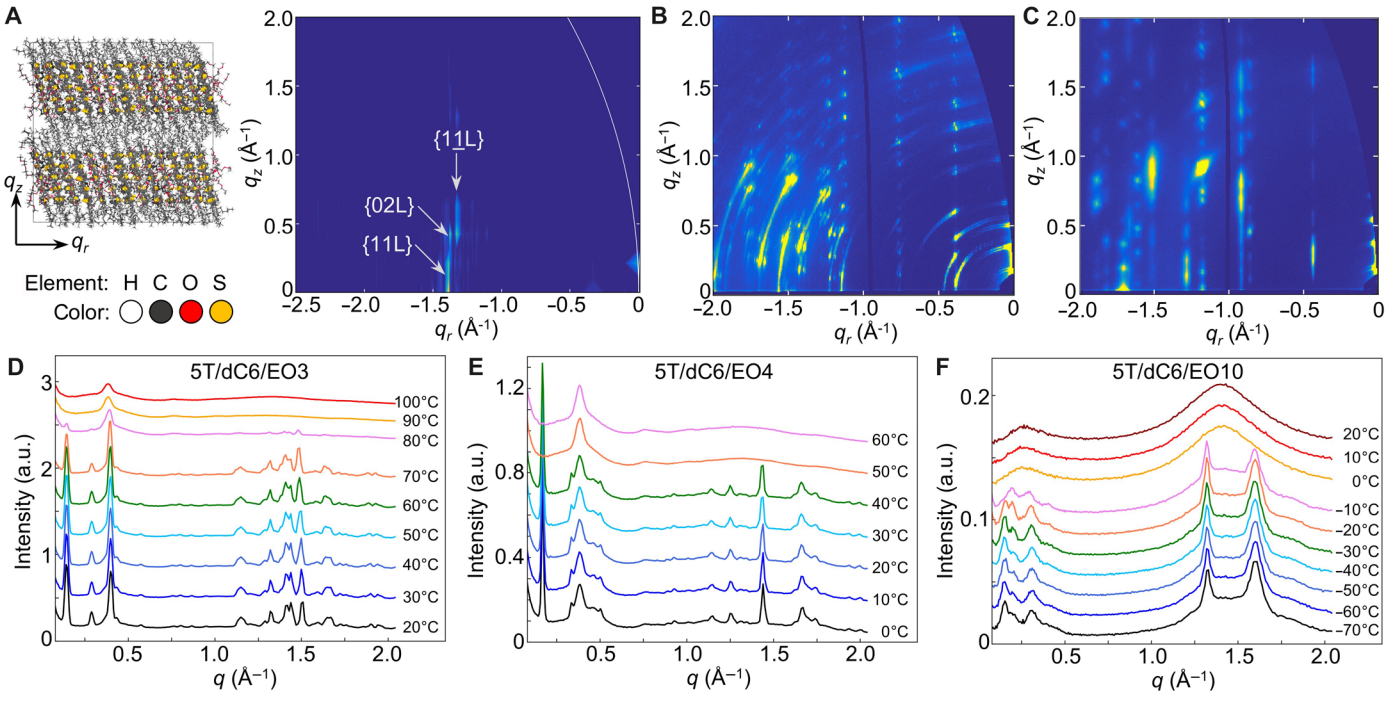


**Fig. 3. Molecular packing of 5T/dC6/EOn.** (**A**) Snapshot of packing morphology of 5T/dC6/EO3 in the all-atom (AA) model representation and the corresponding simulated GIWAXS pattern. Intensities are shown on a linear scale and Miller indices are provided for some diffraction peaks. (**B** and **C**) Experimental GIWAXS patterns of the thin film of 5T/dC6/EO3 and 5T/dC6/EO4 at room temperature. (**D** to **F**) Temperature-dependent WAXS patterns of pristine LC films of 5T/dC6/EO3, 5T/dC6/EO4, and 5T/dC6/EO10, respectively.

dC6/EO10. The film thickness is around 60 to 80 nm. The diffraction peaks in Fig. 3 (B and C) appear qualitatively similar, which can be divided into three parts based on our simulation analysis: the narrow diffraction peaks of (00 $h$) in the out-of-plane direction indicating a lamellar structure parallel to the substrate, the relatively weak peaks at $q_r \approx 0.5$ Å$^{-1}$ representing EOn clusters in each layer, and elongated peaks at larger $q_r$ values indicative of π-π stacking between adjacent 5T units, which played a key role in forming the highly ordered smectic phase.

The temperature-dependent WAXS was conducted for 5T/dC6/EOn during the heating process (Fig. 3, D to F). Both 5T/dC6/EO3 and 5T/dC6/EO4 were measured between 0° and 100°C, below their decomposition temperatures (see fig. S2 in section S1.4), while the 5T/dC6/EO10 film was measured in a lower temperature range from −70° to 20°C. For 5T/dC6/EO3 and 5T/dC6/EO4, two groups of sharp diffraction peaks, including $q < 0.5$ Å$^{-1}$ representing a lamellar structure and $q \approx 1.5$ Å$^{-1}$ representing the π-π stacking among thiophene rings, are observed starting from room temperature. For 5T/dC6/EO10, its diffraction pattern shows relatively weak lamella-related peaks compared to the π-stacking peaks, indicating a different morphology of EOn percolation into the alkyl-thiophene domains. As the temperature increases, all samples undergo an order-disorder transition, indicated by the sudden broadening of diffraction peaks in the vicinity of 80°C for 5T/dC6/EO3, 50°C for 5T/dC6/EO4, and 0°C for 5T/dC6/EO10, which are in good agreement with the DSC results in Fig. 1A. Above the phase transition temperature, 5T/dC6/EO3 and 5T/dC6/EO4 still maintain some remnants of the lamellar structure with the π-π stacking fully disrupted by mobile EOn side chains, while 5T/dC6/EO10 becomes completely disordered.

## Ionic conductivity of 5T/dC6/EOn

The ionic conductivity of 5T/dC6/EOn thin films doped with LiTFSI was measured by electrochemical impedance spectroscopy (EIS) using interdigitated gold electrode (IDE) devices (*47*, *48*) at a salt concentration of $r = [Li^+]/[EO] = 0.05$ over a temperature range from 0° to 140°C through a heating process. Because of the geometry of IDE, the ionic conductivity reported in our work is in-plane conductivity or conductivity in the direction parallel to the substrate. As shown in Fig. 4A, the ionic conductivity of all samples increases with the temperature, and longer EOn side chains can better promote the ionic conductivity. For 5T/dC6/EO3 and 5T/dC6/EO4, their ionic conductivities exhibit a two-stage increase with the temperature due to their order-disorder transition. Here, we would like to note that for the 5T/dC6/EO4 thin-film samples, we were only able to measure conductivity during the first heating cycle due to dewetting issues that occurred at higher temperatures. Therefore, it is possible that the fabricated samples for the first heating cycle were not at equilibrium at low temperature, and the observation of multiple transitions at low temperature is process dependent. At room temperature, EO3 or EO4 side chains form many small ion-conducting clusters dispersed in the alkyl-thiophene domains according to our simulations, and lack of sufficient molecular mobility makes it rather difficult for ions to travel from one cluster to another, resulting in quite low conductivities. When these systems reach the transition temperature, highly ordered LC structures begin to fall apart, and the EO side chains become more and more mobile and easily rearrange to facilitate ion transport, leading to a notable conductivity increase. For example, 5T/dC6/EO4 achieves the maximum observed conductivity around $1.5 \times 10^{-4}$ S/cm at 130°C. For 5T/dC6/EO10, only a disordered structure was observed with no

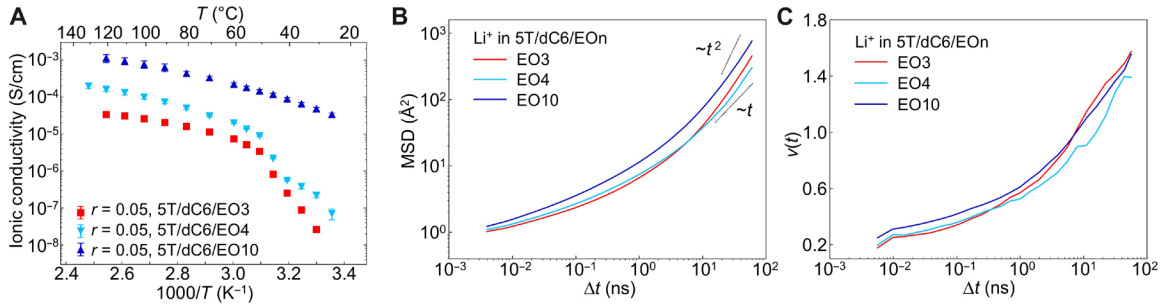


**Fig. 4. Ionic conductivity of 5T/dC6/EOn.** (**A**) Temperature-dependent ionic conductivities of 5T/dC6/EOn doped with LiTFSI at a ratio of $r = 0.05$ measured in experiments. (**B**) Li-ion transport in 5T/dC6/EOn at 400 K and $r = 0.05$ illustrated by MSD curves in simulations. (**C**) Apparent power-law exponents of MSD curves.

phase transition during measurement; thus, the ionic conductivity increases gradually with temperature, reaching the maximum value of $1.1 \times 10^{-3}$ S/cm at 120°C, which is even superior to those nanosegregated ionic LCs (*49*, *50*). The electronic conductivity of oligothiophene in this case, however, is largely disrupted by EOn domains.

Our AA simulations were performed to focus on the impact of the length of EOn segments on Li-ion transport, given the importance of Li-ions as effective charge carriers in processes involving energy conversion and storage for many applications. At our simulated ion concentration of $r = 0.05$, TFSI-ions are expected to show a minimal presence in the Li-ion solvation structure and the Li-ion transport to be largely determined by the interaction between Li-ions and 5T/dC6/EOn molecules (*51*). Incorporating only Li-ions to 5T/dC6/EOn under an electric field allows us to capture the main aspect of the Li-ion transport without simulating the LiTFSI dissociation, and to more efficiently sample the rare but important Li-ion hopping events among EOn segments. In addition, our AA simulations were mainly performed at 400 K, which was consistent with the experimental condition showing a higher conductivity in the disordered molecular structure. Our preliminary results at 300 K (fig. S7) show much slower Li-ion transport due to the reduced dynamics of 5T/dC6/EOn molecules and the isolated EOn clusters in the ordered structures. On the basis of the lamellar structures of 5T/dC6/EO3 and 5T/dC6/EO4 verified by our CG simulations, EOn clusters are dispersed among well-aligned, stationary 5T segments, and the Li-ions are largely trapped within each cluster, considering the lack of structural rearrangement of 5T segments required for Li-ions to travel between different clusters. In contrast, simulations at 400 K allow us to timely observe the transition behavior of Li-ions when traveling around different EOn segments, which is imperative to understand the complex Li-EOn interaction dynamics.

To capture the relative motion of Li-ions with respect to 5T/dC6/EOn molecules, a modified simulation trajectory was generated by subtracting the center of mass of all 5T/dC6/EOn molecules in each frame. Accordingly, the mean-squared displacement (MSD) is calculated for such a trajectory using multiple time origins

$$\mathrm{MSD}(\Delta t) = \frac{1}{\tau_{\mathrm{traj}} - \Delta\tau} \sum_{\tau} \left[ \frac{1}{N} \sum_{i} |\boldsymbol{r}_i(\tau + \Delta\tau) - \boldsymbol{r}_i(\tau)|^2 \right] \quad (1)$$

where $\tau$ is a set of consecutive integers to label successive frames with equal time interval of $\delta t$ in a trajectory, $\Delta\tau$ is the frame interval corresponding to the time of $\Delta t = \Delta\tau \cdot \delta t$, $\tau_{\mathrm{traj}}$ is the total number of frames in a trajectory, $\boldsymbol{r}_i(\tau)$ is the position vector of atom $i$ in frame $\tau$, and $N$ is the number of atoms. Since a charged Li-ion under an electric field is expected to yield a linear response behavior (Ohm's law) (*52*), reaching the regime of MSD ~ $t^2$, the apparent power-law exponent, $\nu$, was calculated by tracking MSD versus $t^{\nu}$ at different times. As shown in Fig. 4 (B and C) and fig. S8, although the Li-ion does not reach the linear-response regime within our computational time, it is already evident from the trends that the Li-ion exhibits the fastest diffusion in 5T/dC6/EO10. In addition, Li-ion diffusion in 5T/dC6/EO3 is slower than that in 5T/dC6/EO4 at short and intermediate times but is faster at long times with larger time-dependent power-law exponents. For the same ion-doping ratio of $r = 0.05$, the number density of Li-ion in 5T/dC6/EOn varies with the length of EOn segment. For comparison, a normalized ionic conductivity ($\Lambda_{\mathrm{ion}}$) is then approximated by the product of the Li-ion density ($\rho_{\mathrm{ion}}$) and apparent Li-ion diffusivity ($D_{\mathrm{app}}$) evaluated with the Einstein relation at 60 ns (Table 1). Overall, ion-doped 5T/dC6/EO10 shows the highest conductivity due to the fastest diffusion and highest density of Li-ions. Compared to 5T/dC6/EO4, ion-doped 5T/dC6/EO3 has lower Li-ion density but faster Li-ion diffusion, leading to an overall ionic conductivity which is slightly higher. Here, our simulated conductivity trend for 5T/dC6/EO3 and 5T/dC6/EO4 is inconsistent with the experimental data, likely related to our limited computation times and simulation setup without TFSI-ions. Notwithstanding this shortcoming, our subsequent analysis of the

**Table 1. Normalized ionic conductivity in 5T/dC6/EOn at 400 K.**

| System | $D_{\mathrm{app}}$(60 ns)/(Å$^2$·ns$^{-1}$) | $\rho_{\mathrm{ion}}$/nm$^{-3}$ | $\Lambda_{\mathrm{ion}}$ (normalized) |
|---|---|---|---|
| 5T/dC6/EO3 | 1.25 | 0.139 | 1.00 |
| 5T/dC6/EO4 | 0.83 | 0.172 | 0.82 |
| 5T/dC6/EO10 | 2.10 | 0.312 | 3.77 |

Li-ion solvation environment can still be instructive for revealing the transport mechanism and to further establish material design strategies.

To characterize the interaction between Li-ion and oxygen, the pair radial distribution function (RDF) is calculated by the ratio between local and bulk number density of oxygen atoms around Li-ions, $\rho_O(r)$ and $\rho_O$

$$g_{Li-O}(r) = \frac{\langle \rho_O(r) \rangle}{\rho_O} = \frac{V}{N_{Li} N_O} \left\langle \sum_{i \in Li} \sum_{j \in O} \delta\left(r - \|\boldsymbol{r}_i - \boldsymbol{r}_j\|\right) \right\rangle \quad (2)$$

where $r$ is a given separation distance, $\boldsymbol{r}_i$ and $\boldsymbol{r}_j$ are the position vector of a Li-ion and an oxygen atom, $\delta(\cdots)$ is the Dirac delta function, $\|\cdots\|$ denotes the Euclidean distance, $\langle X(r) \rangle$ denotes the ensemble average of a radially varying property given by $X(r)$, $V$ is the volume of the simulation box, $N_{Li}$ and $N_O$ are the numbers of Li-ions and oxygen atoms in the system. In practice, rather than the delta function, $\rho_O(r)$ is computed from a histogram using a spherical shell at a radial distance $r$ and thickness d$r$. In addition, the cumulative RDF (CRDF) directly shows the cumulative number of oxygen atoms within a distance from the Li-ion.

### *A Li-ion is solvated by roughly six coordinating oxygens from the same or different EO segments/molecules*

The Li-ion solvation shell is formed by the group of oxygen atoms within the first peak of RDF, and the shell radius is determined by the minimum between the first two peaks. In 5T/dC6/EOn, solvation shells show similar features consisting roughly of six oxygen atoms according to CRDF with a radius around 3.4 Å (Fig. 5, A and B). Different solvation motifs were distinguished on the basis of three numbers: the number of oxygen atoms, EO segments, and 5T/dC6/EOn molecules participating in the solvation shell. Here, a solvating segment is defined as a set of contiguous EO units from the same molecule. Figure 5C shows the frequency of different motifs observed in simulations. In 5T/dC6/EO3 and 5T/dC6/EO4, the primary motif is 6-2-2, where a Li-ion is coordinated by six oxygen atoms coming from two EOn segments adopting a crisscross conformation (Fig. 5D). In 5T/dC6/EO10, other than the 6-2-2 motif, 6-1-1 and 7-1-1 motifs also occur with appreciable frequencies, where a Li-ion is coordinated by a single segment with six or seven contiguous EO units adopting a helical conformation (Fig. 5E and fig. S9). Oxygen atoms not within any Li-ion shell are denoted as "free" for our ensuing discussion. A small peak observed in the RDFs of 5T/dC6/EO4 and 5T/dC6/EO10 at 4.25 Å (Fig. 5A) likely corresponds to nearby free oxygen atoms within those EOn segments coordinating Li-ions; this is not observed for 5T/dC6/EO3 where all three oxygen atoms from a solvating segment are often needed to coordinate a Li-ion, leaving no nearby free oxygen. The peak in RDF at 6.15 Å (Fig. 5A) can be associated with free oxygen atoms from other nonsolvating molecules, and the slope of CRDF beyond 5 Å basically reflects the average oxygen density in 5T/dC6/EOn.

### *Changes in solvation shell over time reveal roles of inter- and intrachain hopping events*

The Li-ion transport mechanism is investigated by tracking the changes of the Li-ion solvation shell with time. Here, each oxygen atom in the system is labeled consecutively with a unique index. Given a Li-ion $i$ at a time $t$, $SH_i(t)$ is defined as a list of oxygen indices within its solvation shell. When comparing constituent oxygen atoms of a solvation shell at two different times, we can classify three

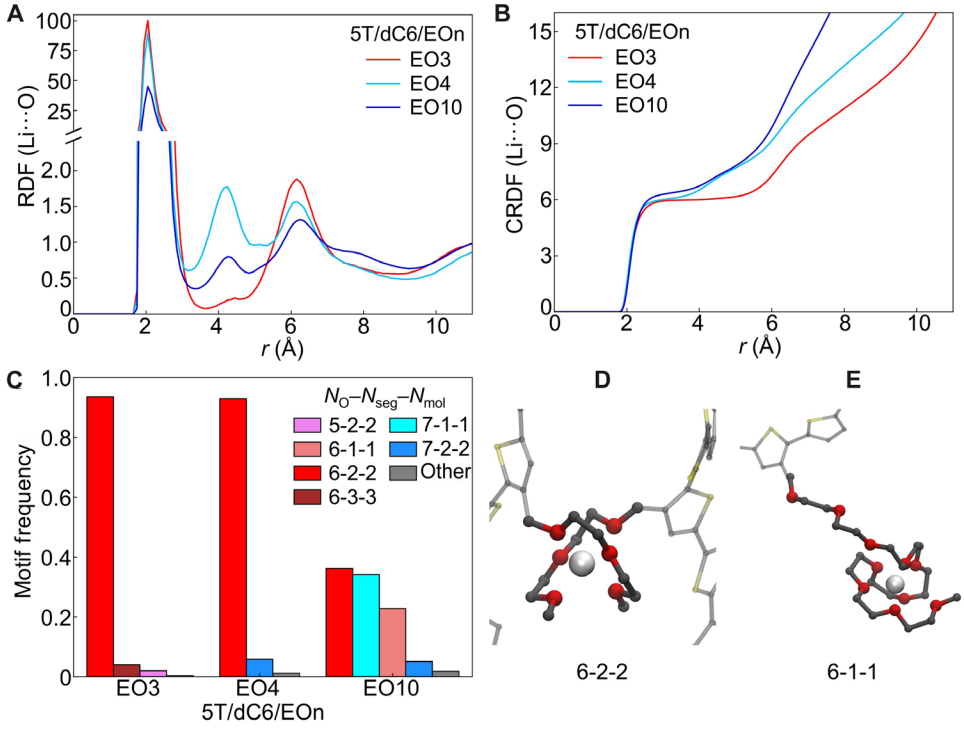


**Fig. 5. Li-ion solvation shell in 5T/dC6/EOn.** (**A**) Radial distribution function and (**B**) related cumulative function of oxygen atoms around Li-ions. (**C**) Frequency of observed Li-ion solvation motifs. (**D** and **E**) Snapshots of representative Li-ion solvation motifs. Li-ions are colored in white, carbon atoms in gray, oxygen atoms in red, and sulfur atoms in yellow. For clarity, hydrogen atoms are omitted, and 5T/dC6 backbones are cropped and shown partially transparent.

oxygen categories: atom leaving, staying in, and entering the shell as shown in Fig. 6A. Furthermore, the time autocorrelation function of the Li-ion solvation shell (TACF-SH) (*30*, *31*, *51*, *53*, *54*) is calculated and normalized for different oxygen categories using multiple time origins. The TACF-SH of "staying" oxygen atoms is calculated to quantify the solvation/residence time of oxygen with Li-ion

$$\mathrm{TACF-SH_{stay}}(\Delta t) = \frac{1}{\tau_{\mathrm{traj}} - \Delta\tau} \sum_{\tau} \left[ \frac{1}{N_{\mathrm{Li}}} \sum_{i} \frac{|\mathrm{SH}_i(\tau) \cap \mathrm{SH}_i(\tau + \Delta\tau)|}{|\mathrm{SH}_i(\tau)|} \right] \quad (3)$$

where $t$ and $\tau$ are used to label time and frame in a simulation trajectory as mentioned in Eq. 1, $\cap$ is the intersection operator, $|\cdots|$ is the cardinality (number of elements) of a set, and $N_{\mathrm{Li}}$ is the number of Li-ions in the system. TACF-SH$_{\mathrm{stay}}$ takes on a value from 1 for no change to 0 for complete change in the solvation shell. Overall, oxygen atoms in 5T/dC6/EO4 coordinate Li-ions for much longer time with a flat decay in TACF-SH$_{\mathrm{stay}}$ than the other two systems (Fig. 6B). Closer inspection also reveals that both 5T/dC6/EO4 and 5T/dC6/EO10 exhibit a two-stage decay in TACF-SH$_{\mathrm{stay}}$, where a fast decay with a steep slope occurs at small times followed by a slow decay, while 5T/dC6/EO3 is dominated by a single-slope decay.

The TACF-SH of "entering" oxygen atoms is calculated to examine different ion hopping events

$$\mathrm{TACF-SH_{enter}}(\Delta t) = \frac{1}{\tau_{\mathrm{traj}} - \Delta\tau} \sum_{\tau} \left[ \frac{1}{N_{\mathrm{Li}}} \sum_{i} \frac{|\mathrm{SH}_i(\tau + \Delta\tau) \backslash \mathrm{SH}_i(\tau)|}{|\mathrm{SH}_i(\tau + \Delta\tau)|} \right] \quad (4)$$

where \ is the set difference operator. TACF-SH$_{\mathrm{enter}}$ takes on a value from 0 for no change to 1 for complete change in the solvation shell. The entering atoms can be divided into two groups associated with either intrachain or interchain hopping as shown in Fig. 6C based on whether they are from the same EOn segment of "leaving" and "staying" atoms. In 5T/dC6/EO3, interchain hopping contributes to almost all changes of the solvation shell, which is consistent with the single-slope decay of TACF-SH$_{\mathrm{stay}}$. In 5T/dC6/EO4, while intrachain hopping makes the primary contribution to the fast decay in TACF-SH$_{\mathrm{stay}}$ at short times, the slow interchain hopping results in very limited changes to the solvation shell at long times. Li-ions in 5T/dC6/EO3 show faster interchain hopping than 5T/dC6/EO4, which is consistent with the higher Li-ion mobility in the former as quantified by the MSD data. For the dominant Li-ion solvation motif of 6-2-2 in 5T/dC6/EO3 (Fig. 5C), a Li-ion is coordinated by two EO3 segments with all six oxygens, effectively precluding intrachain hopping. For the 6-2-2 motif in 5T/dC6/EO4, a Li-ion is coordinated by two EO4 segments, leaving two free oxygen atoms outside the solvation shell to facilitate the intrachain hopping, and these two oxygen atoms appear to establish an extra barrier for the Li-ion to escape from its existing solvation environment through proper interchain hopping. Furthermore, two EO4 segments can shield a Li-ion more thoroughly than two EO3 segments, and TFSI-ions are expected to move more freely in 5T/dC6/EO4 than in 5T/dC6/EO3, which likely accounts for the discrepancy between experimental and computational conductivity data. The higher ionic conductivity of 5T/dC6/EO4 observed in experiments could reflect the motion of TFSI-ions. In 5T/dC6/EO10, intrachain hopping mainly contributes to the initial fast decay of TACF-SH$_{\mathrm{stay}}$, while interchain hopping plays a major role in the decorrelation of the solvation shell composition over the longer time scales relevant to ionic transport. Among the three 5T/dC6/EOn systems, Li-ions in 5T/dC6/EO10 show the fastest interchain hopping, consistent with their highest Li-ion mobility. Examples of ion hopping are shown in figs. S10 and S11 from section S4.2 with complementary details.

### *Potential Li-ion solvation sites in 5T/dC6/EO10 are more densely distributed and in closer proximity*

Apart from the local solvation environment of Li-ion, it is of great interest to examine the overall long-range spatial structure of ion-conducting domains formed by EOn segments. The concept of solvation sites (*55*–*57*) has been developed to identify possible locations

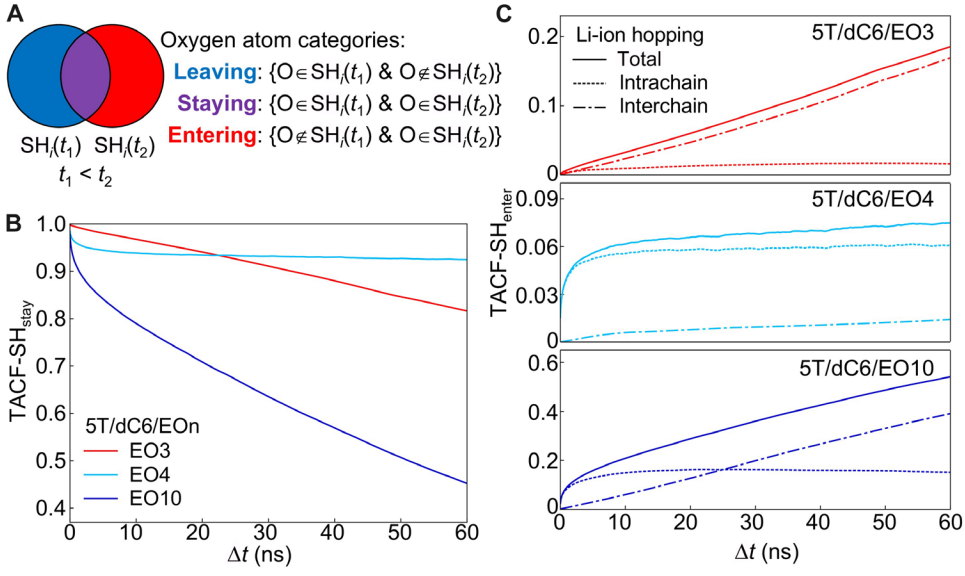


**Fig. 6. Dynamics of Li-ion solvation shell in 5T/dC6/EOn.** (**A**) Categorization of oxygen atoms in the solvation shell according to their dynamic behavior. (**B**) TACF-SH for oxygen atoms staying in the shell. (**C**) TACF-SH for oxygen atoms related to Li-ion hopping. Curves for Li-ion hopping types are depicted by different line styles and molecular systems by different colors.

in the conduction domains capable of fully coordinating Li-ions, which can serve as a useful, albeit approximate metric to quantify the abundance of such sites and the ease of potential Li-ion hopping events among them. To be consistent with the prevalent solvation motifs found in Fig. 5, the solvation site is defined as the centroid of a set of six or more oxygen atoms if each of which is also within a threshold distance around the centroid; this threshold distance ($r_{site}$) is set to be the radius of Li-ion solvation shell determined by RDF, $r_{site}$ = 3.4 Å. An algorithm to identify possible solvation sites in a simulated configuration is presented in section S4.3.

Among the three 5T/dC6/EOn systems, solvation sites were found to be more densely distributed in the system with a higher volume fraction of EOn segments, i.e., the $n$ = 10 case (Fig. 7A). To give an approximate visualization of available hopping events, any pair of sites closer than a limiting hopping distance of 3 Å (*57*) is connected by an edge. This precise choice of limiting hopping distance is not essential to sort out the trends in our ensuing results, but it is a convenient value that follows the analysis of a prior study (*57*), as being able to capture the rapidly increasing barrier to hopping with intersite distance. The average nearest-neighbor distance for solvation sites is calculated as

$$\langle r_{nn} \rangle = \left\langle \frac{1}{N_{site}} \sum_{i} \min_{j \neq i} (r_{ij}) \right\rangle \quad (5)$$

where $N_{site}$ is the number of solvation sites identified in a simulated configuration, $r_{ij}$ is the distance between two sites $i$ and $j$, and $\langle \cdots \rangle$ denotes the ensemble average over a trajectory. Our simulations show that the edge density in 5T/dC6/EO3 is less than the corresponding bulk site density (Table 2) indicating limited connection among sites. In contrast, in both 5T/dC6/EO4 and 5T/dC6/EO10, the edge site density is higher, indicating better-connected site networks. Results in Table 2 indicate that $\langle r_{nn} \rangle$ in 5T/dC6/EO4 and 5T/dC6/EO10 are comparable but distinctly smaller than $\langle r_{nn} \rangle$ in 5T/dC6/

**Table 2. Characterization of solvation sites in 5T/dC6/EOn.**

| System | $\rho_{site}$/nm$^{-3}$ | $\rho_{edge}$/nm$^{-3}$ | $\langle r_{nn} \rangle$/Å |
|---|---|---|---|
| 5T/dC6/EO3 | 0.162 | 0.041 | 10.88 |
| 5T/dC6/EO4 | 0.486 | 0.677 | 2.23 |
| 5T/dC6/EO10 | 0.951 | 1.482 | 2.05 |

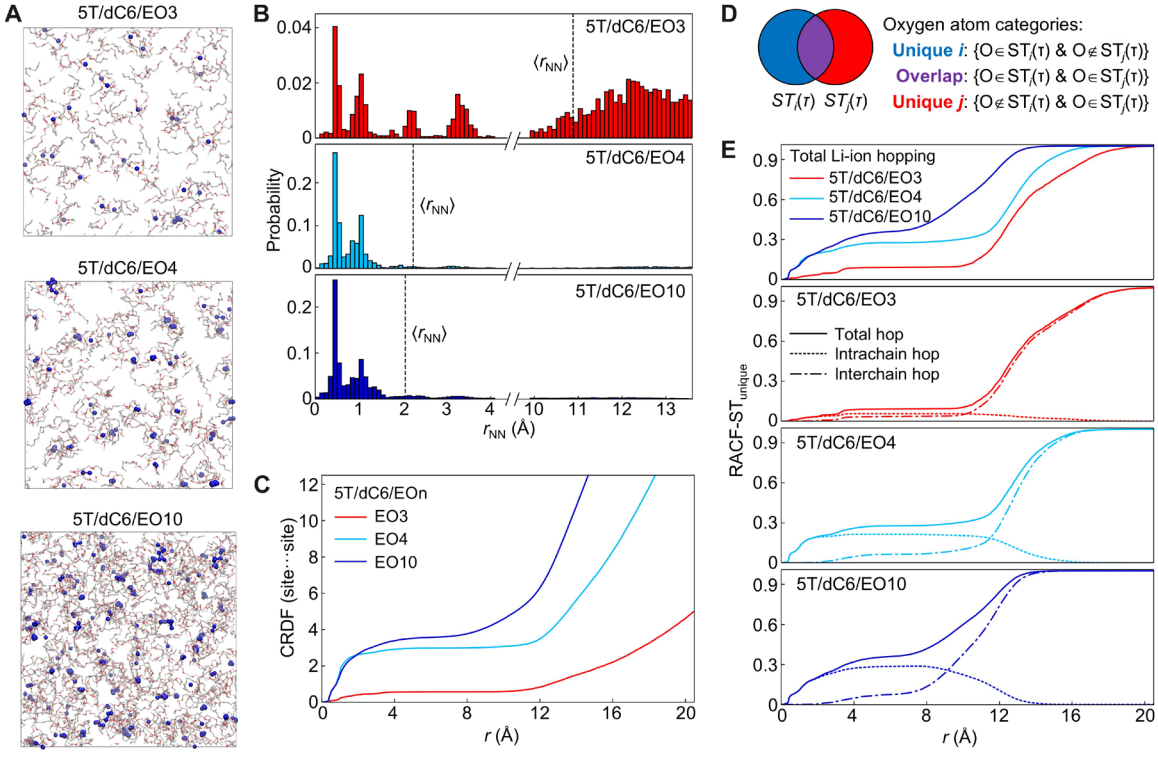


**Fig. 7. Distribution of solvation sites in 5T/dC6/EOn.** (**A**) Representative snapshots of solvation sites in the 5T/dC6/EOn. Sites are depicted by blue spheres, and edges between sites within 3 Å are depicted by blue bonds. EOn segments are shown in the transparent representation with carbon in white and oxygen in red. (**B**) Distribution of the nearest-neighbor distances for individual solvation sites, where the average value is marked by a dotted line. (**C**) Cumulative RDFs between solvation sites. (**D**) Categorization of oxygen atoms based on their associated solvation sites. (**E**) Radial autocorrelation function of solvation site (RACF-ST) for oxygen atoms related to potential hopping events. Curves for hopping types are depicted by different line styles and molecular systems by different colors.

EO3. Distributions of $r_{nn}$ (Fig. 7B) reveal that a considerable portion of sites in 5T/dC6/EO3 are separated from their neighbors by at least 10 Å, while sites in 5T/dC6/EO4 and 5T/dC6/EO10 are often within 4 Å of a neighbor site. Furthermore, the site-site CRDF of 5T/dC6/EO3 (Fig. 7C) shows that sites only find at most one neighbor with a long plateau region up to 9.7 Å, suggesting the presence of many isolated sites. In contrast, the CRDFs of 5T/dC6/EO4 and 5T/dC6/EO10 show that local clusters contain three to four sites with a radius of around 2.5 Å, with the following plateau region serving as a metric of the cluster-to-cluster distance. Site clusters in 5T/dC6/EO10 are more densely distributed with the smallest intercluster distance.

### *Solvation intersite lengths can be associated with ion hopping times*

To connect solvation site networks with potential ion hopping events, different sites are first classified on the basis of their associated oxygen atoms. Given a configuration $\tau$, $ST_i(\tau)$ denotes a list of oxygen indices linked to site $i$. When comparing sites $i$ and $j$, their associated atoms can be divided into three categories: overlap (if shared by at least two sites), unique to site $i$, and unique to site $j$ (Fig. 7D). To estimate the transport length of ion hopping, the radial autocorrelation function of solvation site (RACF-ST) is calculated and normalized for "unique" atoms

$$\mathrm{RACF-ST_{unique}}(r) = \frac{1}{\tau_{\mathrm{traj}}}\sum_{\tau}\left\{\frac{1}{N_{\mathrm{site}}}\sum_{i}\max_{j\neq i}\left[\frac{\mathrm{ST}_j(\tau)\backslash ST_i(\tau)}{ST_j(\tau)}, \text{if } r_{ij}<r\right]\right\} \quad (6)$$

where $\tau_{\mathrm{traj}}$ is the number of configurations used to identify solvation sites, and $r_{ij}$ is the distance between sites $i$ and $j$. Taking a site $i$ as the reference, the ratio of unique atoms is calculated for any site $j$ within a distance from site $i$, and the site with the maximum ratio is chosen for RACF-ST to give a lower limit for the transport length (fig. S12). RACF-$\mathrm{ST_{unique}}$ takes on a value from 0 for no change to 1 for complete change of site-associated atoms. Also, unique atoms of site $j$ can be divided into two groups related to intrachain and interchain hopping depending on whether they are from the same EOn segments as atoms of site $i$ (Fig. 7E). In 5T/dC6/EO3, interchain hopping would be the primary mechanism for a Li-ion to jump from site to site, with a Li-ion needing to travel at least 9.7 Å up to 20.3 Å to change its coordinating oxygen atoms. In 5T/dC6/EO4, a Li-ion can jump to neighboring sites only within 2 Å through intrachain hopping; however, it needs to travel around 11.3 to 18.2 Å to substantially alter its surrounding oxygen atoms through interchain hopping. In 5T/dC6/EO10, the transport length for intrachain hopping is less than 3.7 Å, and the length for interchain hopping is about 7.3 to 15.4 Å, smaller than that for the other two systems. Comparing TACF of Li-ion solvation shell with RACF of solvation site, the lack of intrachain hopping in 5T/dC6/EO3 is related to a large portion of isolated sites, while fast intrachain hopping in 5T/dC6/EO4 and 5T/dC6/EO10 arises from the small transport length around 3 Å to available nearby sites. Interchain hopping, which can completely alter the composition of the Li-ion solvation shell, usually occurs at longer times given the larger transport length between solvation sites with quite different oxygen compositions, and faster interchain hopping usually correlates with smaller transport lengths. In summary, the highest ionic conductivity of 5T/dC6/EO10 observed in both experiments and simulations can be attributed to the fastest interchain hopping associated with the smallest transport length between solvation sites. Moreover, in our simulations, Li-ions exhibit enhanced mobility in 5T/dC6/EO3 compared to 5T/dC6/EO4, which is also related to the rate of interchain hopping and the required transport length.

## DISCUSSION

We conducted an integrated approach of experiments and simulations to study the self-assembly and ionic conductivity of a series of synthesized T-shaped polyphilic LC molecules, 5T/dC5/EOn. The thermal behavior of these compounds confirmed that the order-disorder transition temperature decreases as the length of the EOn side chain increases. CG simulations helped reveal molecular packing details in the ordered structures, namely, that the molecule with a short EOn side-chain forms a lamellar phase with many small EOn clusters dispersed in thiophene domains, while the molecule with a long EOn side chain forms a columnar phase containing multiple continuous EOn domains.

EIS measurements on 5T/dC6/EOn films showed that longer EOn side chains can promote ion transport with the highest conductivity of $1.1 \times 10^{-3}$ S/cm observed for 5T/dC6/EO10 at 120°C. The Li-ion solvation shell was characterized by atomistic simulations to understand the transport mechanism. Our simulations reveal that the Li-ion transport in the molecule with a short EOn side chain exhibited a lack of necessary intrachain hopping and relatively slow interchain hopping, leading to a long coordinating time of the oxygen atom with the Li-ion. The improved ion-conducting performance in 5T/dC6/EO10 is largely related to a balanced combination of intrachain hopping at short times followed by interchain hopping at long times. Solvation site networks were constructed in the ion-conducting EOn domains to identify potential hopping events. For 5T/dC6/EO3 and 5T/dC6/EO4, the large proportion of isolated solvation sites or small site clusters implies a long travel distance for interchain hopping, while for 5T/dC6/EO10, the densely distributed site clusters are expected to lower the activation barrier to enact frequent interchain hopping events. In summary, our simulations reveal a correlation between molecular design, mesophase morphology, domain size, and connectivity of ion-conducting domains with Li-ion transport mechanisms; the nonmonotonic trends in ionic conductivity with the length $n$ of the EOn segments highlights the nontrivial coupling of EO domain geometry and intra- versus interchain Li-ion hopping events.

In terms of molecular design, our results proved that the combination of the T-shaped facial polyphilic molecules with a charge-conducting functionality can induce complex mesophases with confined charge transport channels. Furthermore, our simulations indicate that a suitable length of the EOn segment in 5T/dC6/EOn can be favorable to Li-ion transport. For example, one 5T/dC6/EO10 molecule can properly surround a Li-ion using six oxygen atoms, with the four extra oxygen atoms providing adequate molecular flexibility to facilitate the conformational rearrangements entailed by ion hopping and to serve as a bridge to connect to other free EO10 segments. By contrast, two 5T/dC6/EO4 molecules can thoroughly coordinate a Li-ion using six oxygen atoms, with the two extra oxygen atoms hindering interchain hopping due to their limited flexibility.

It is remarkable that for the systems studied, the ordered, liquid crystalline morphologies of our 5T/dC6/EOn molecules did not prove to be the most advantageous for ionic conductivity, and one could question whether a different ordered phase may have been more effective. Here, we note that similar three-block T-shaped molecular designs exhibit remarkable phase diversity, extending beyond lamellar, columnar, and honeycomb phases (*40*–*42*). The complex T-shaped molecular architecture, with its inherent shape

anisotropy and structural versatility, facilitates the stabilization of network phases across a wide range of conditions. Moreover, at intermediate temperatures, these systems form disordered network morphologies rather than fully isotropic phases, where different constituent chemical blocks nanosegregate into interconnected domains percolating throughout the entire sample. The three-dimensional percolating domains in these network morphologies, maintained across ordered and disordered states over wide temperature ranges, could provide enhanced ion/electron conduction due to their inherent resilience against the detrimental effects of grain boundaries and structural defects (which often compromise conductivity in typical ordered LC morphologies). In this sense, they may embody a paradigm shift in what the target ion/electron-conducting morphology should be when designing small mesogenic molecules. While we chose to focus on the relation between varying structures and ionic conductivity, more work is needed to understand the relation between structure and electronic conductivity. Despite the diminished electronic transport of our molecules due to EOn clustering, future refinements of this T-shaped molecular design (e.g., targeting network transport pathways) have significant potential for developing materials with strong mixed ionic/electronic conductivity. For example, future work can aim to achieve self-assembled structures that optimally balance long-range positional order with localized disorder (i.e., imparting "plastic crystalline" properties), where long-range order can establish continuous pathways for efficient electronic conduction, while localized disorder enables limited yet sufficient structural rearrangement to facilitate ion hopping between molecules (*58*).

## MATERIALS AND METHODS

### Materials and synthesis

All reagents and solvents were purchased from AK Scientific, Sigma-Aldrich, Thermo Fisher Scientific, and Honeywell, which were used as received unless otherwise noted. Anhydrous tetrahydrofuran (THF) was freshly distilled from sodium and benzophenone before use. *N*-bromosuccinimide was recrystallized in water and stored in refrigerator before use. The synthetic procedure and characterization of 5T/dC6/EOn are provided in section S1.2.

### Nuclear magnetic resonance

$^{1}$H and $^{13}$C NMR spectra were recorded on a Varian INOVA 400 and a MERCURY 300 spectrometers. Chemical shifts were quoted relative to the residual protons of the deuterated solvents $CDCl_3$ ($\delta = 7.26$ for $^{1}$H and $\delta = 77.36$ for $^{13}$C). The multiplicity was characterized by the following abbreviations: singlet (s), doublet (d), triplet (t), quartet (q), and multiplet (m).

### Preparation of 5T/dC6/EOn-LiTFSI blend samples

Solutions of 5T/dC6/EOn and LiTFSI (Sigma-Aldrich, battery grade) were prepared separately by dissolving the materials in anhydrous THF at a concentration of 10 mg·ml$^{-1}$ each and fully shaken using a vortexer before mixing. 5T/dC6/EOn and LiTFSI solutions were then mixed at the appropriate ratios to achieve the concentrations $r = [Li^+]/[EO] = 0.05$. DSC and POM images were taken on bulk 5T/dC6/EOn-LiTFSI complexes prepared by slow evaporation of the mixed 5T/dC6/EOn-LiTFSI solution at 80°C followed by drying under vacuum for 24 hours at 80°C.

### Differential scanning calorimetry

DSC measurements were performed on a Q 2000 from TA Instruments at a scanning rate of 10°C/min within a temperature range from −90° to 200°C. The phase transition temperatures were determined as the peak positions in the DSC traces due to broadness of the transition peaks.

### Polarized optical microscope

An Olympus BX51 equipped with a Mettler FP 82 HT hot stage was used for visual observation of optical textures at different temperatures.

### Temperature-dependent WAXS

T-dependent WAXS was performed with SAXSLAB (XENOCS)'s GANESHA equipped with a T-95 Linkam stage at the University of Chicago X-ray Facility. Measurement details are provided in section S1.3.

### Grazing-incidence wide-angle x-ray scattering

GIWAXS were performed at beamline 8-ID-E of the Advanced Photon Source, Argonne National Laboratory with 10.86 keV ($\lambda = 1.1416$ Å) synchrotron radiation. Measurement details are provided in section S1.3.

### Simulation method

To timely observe the self-assembly of oligomeric LCs given our accessible computational resources, a CG model of 5T/dC6/EOn was used to generate representative realization of their complex mesophases. However, to study ionic conduction, an AA model (*26*, *59*) of 5T/dC6/EOn was implemented to provide necessary atomistic details that capture the relevant energetic and steric barriers to ionic mobility; the AA model configurations were obtained by first inverse mapping from well-equilibrated CG ones and then allowing them to thermally equilibrate. The solvation environment of Li-ions was examined to understand their transport in the conduction domains of EOn side chains, whose morphologies were further characterized by the solvation-site network approach. Force field parameters and simulation details are provided in section S2 with figs. S3 and S4. All the simulations were performed using Large-scale Atomic/Molecular Massively Parallel Simulator (LAMMPS) simulation package (*60*, *61*) with Graphics Processing Unit (GPU) acceleration (*62*, *63*), and Visual Molecular Dynamics (VMD) (*64*) was used for visualizations.

### Conductivity measurement

EIS conductivity measurements were performed on samples fabricated on top of nanofabricated IDE devices using a Gamry 600+ Potentiostat inside a nitrogen-filled glovebox. Before EIS measurement, the excess amount of materials on the electrode pads was scraped away to make electrical connection to the sample. The electrical connection was made using two-probe manipulators (Semiprobe Inc.). The EIS characterization was performed from 1 MHz to 0.1 Hz with an oscillatory peak potential of 100 mV. EIS measurement was carried out at different temperatures controlled by a benchtop heater controller (Omega Engineering Inc.). The collected impedance data were then fit to appropriate equivalent circuits to extract the sample ionic resistance $R_{ion}$ and then ionic conductivity. More details can be found in our previous publication (*65*).

## Supplementary Materials

**This PDF file includes:**

Supplementary Text
Figs. S1 to S12
Tables S1 to S13
References

## REFERENCES AND NOTES


1. S. Allard, M. Forster, B. Souharce, H. Thiem, U. Scherf, Organic semiconductors for solution-processable field-effect transistors (OFETs). *Angew. Chem. Int. Ed. Engl.* **47**, 4070–4098 (2008).
2. S. Sergeyev, W. Pisula, Y. H. Geerts, Discotic liquid crystals: A new generation of organic semiconductors. *Chem. Soc. Rev.* **36**, 1902–1929 (2007).
3. F. Huang, H. Wu, Y. Cao, Water/alcohol soluble conjugated polymers as highly efficient electron transporting/injection layer in optoelectronic devices. *Chem. Soc. Rev.* **39**, 2500–2521 (2010).
4. M. Funahashi, Development of liquid-crystalline semiconductors with high carrier mobilities and their application to thin-film transistors. *Polym. J.* **41**, 459–469 (2009).
5. W. Pisula, M. Zorn, J. Y. Chang, K. Müllen, R. Zentel, Liquid crystalline ordering and charge transport in semiconducting materials. *Macromol. Rapid Commun.* **30**, 1179–1202 (2009).
6. L. Schmidt-Mende, A. Fechtenkötter, K. Müllen, E. Moons, R. H. Friend, J. D. MacKenzie, Self-organized discotic liquid crystals for high-efficiency organic photovoltaics. *Science* **293**, 1119–1122 (2001).
7. T. Hori, Y. Miyake, N. Yamasaki, H. Yoshida, A. Fujii, Y. Shimizu, M. Ozaki, Solution processable organic solar cell based on bulk heterojunction utilizing phthalocyanine derivative. *Appl. Phys. Express* **3**, 101602 (2010).
8. W. Shin, T. Yasuda, G. Watanabe, Y. S. Yang, C. Adachi, Self-organizing mesomorphic diketopyrrolopyrrole derivatives for efficient solution-processed organic solar cells. *Chem. Mater.* **25**, 2549–2556 (2013).
9. A. Seki, K. Shimizu, K. Aoki, Chiral π-conjugated liquid crystals: Impacts of ethynyl linker and bilateral symmetry on the molecular packing and functions. *Crystals* **12**, 1278 (2022).
10. A. E. A. Contoret, S. R. Farrar, P. O. Jackson, S. M. Khan, L. May, M. O'Neill, J. E. Nicholls, S. M. Kelly, G. J. Richards, Polarized electroluminescence from an anisotropic nematic network on a non-contact photoalignment layer. *Adv. Mater.* **12**, 971–974 (2000).
11. T. Hassheider, S. A. Benning, H. S. Kitzerow, M. F. Achard, H. Bock, Color-tuned electroluminescence from columnar liquid crystalline alkyl arenecarboxylates. *Angew. Chem. Int. Ed. Engl.* **40**, 2060–2063 (2001).
12. S. A. Benning, R. Oesterhaus, H. Kitzerow, Polarized electroluminescence of a discotic mesogenic compound. *Liq. Cryst.* **31**, 201–205 (2004).
13. M. P. Aldred, A. E. A. Contoret, S. R. Farrar, S. M. Kelly, D. Mathieson, M. O'Neill, W. C. Tsoi, P. Vlachos, A full-color electroluminescent device and patterned photoalignment using light-emitting liquid crystals. *Adv. Mater.* **17**, 1368–1372 (2005).
14. A. J. J. M. van Breemen, P. T. Herwig, C. H. T. Chlon, J. Sweelssen, H. F. M. Schoo, S. Setayesh, W. M. Hardeman, C. A. Martin, D. M. de Leeuw, J. J. P. Valeton, C. W. M. Bastiaansen, D. J. Broer, A. R. Popa-Merticaru, S. C. J. Meskers, Large area liquid crystal monodomain field-effect transistors. *J. Am. Chem. Soc.* **128**, 2336–2345 (2006).
15. M. Funahashi, F. Zhang, N. Tamaoki, High ambipolar mobility in a highly ordered smectic phase of a dialkylphenylterthiophene derivative that can be applied to solution-processed organic field-effect transistors. *Adv. Mater.* **19**, 353–358 (2007).
16. Y. Shimizu, K. Oikawa, K. Nakayama, D. Guillon, Mesophase semiconductors in field effect transistors. *J. Mater. Chem.* **17**, 4223–4229 (2007).
17. W. Pisula, A. Menon, M. Stepputat, I. Lieberwirth, U. Kolb, A. Tracz, H. Sirringhaus, T. Pakula, K. Müllen, A zone-casting technique for device fabrication of field-effect transistors based on discotic hexa-*peri*-hexabenzocoronene. *Adv. Mater.* **17**, 684–689 (2005).
18. J. C. Maunoury, J. R. Howse, N. L. Turner, Melt-processing of conjugated liquid crystals: A simple route to fabricate OFETs. *Adv. Mater.* **19**, 805–809 (2007).
19. H. Monobe, K. Awazu, Y. Shimizu, Change of liquid-crystal domains by vibrational excitation for a columnar mesophase. *Adv. Mater.* **12**, 1495–1499 (2000).
20. A. Tracz, J. K. Jeszka, M. D. Watson, W. Pisula, K. Müllen, T. Pakula, Uniaxial alignment of the columnar super-structure of a hexa (alkyl) hexa-*peri*-hexabenzocoronene on untreated glass by simple solution processing. *J. Am. Chem. Soc.* **125**, 1682–1683 (2003).
21. V. De Cupere, J. Tant, P. Viville, R. Lazzaroni, W. Osikowicz, W. R. Salaneck, Y. H. Geerts, Effect of interfaces on the alignment of a discotic liquid−crystalline phthalocyanine. *Langmuir* **22**, 7798–7806 (2006).
22. Y. Sagara, T. Kato, Mechanically induced luminescence changes in molecular assemblies. *Nat. Chem.* **1**, 605–610 (2009).
23. T. Kato, M. Yoshio, T. Ichikawa, B. Soberats, H. Ohno, M. Funahashi, Transport of ions and electrons in nanostructured liquid crystals. *Nat. Rev. Mater.* **2**, 17001 (2017).
24. S. Yazaki, M. Funahashi, J. Kagimoto, H. Ohno, T. Kato, Nanostructured liquid crystals combining ionic and electronic functions. *J. Am. Chem. Soc.* **132**, 7702–7708 (2010).
25. B. D. Paulsen, K. Tybrandt, E. Stavrinidou, J. Rivnay, Organic mixed ionic–electronic conductors. *Nat. Mater.* **19**, 13–26 (2020).
26. Z. Liu, B. X. Dong, M. Misra, Y. Sun, J. Strzalka, S. N. Patel, F. A. Escobedo, P. F. Nealey, C. K. Ober, Self-assembly behavior of an oligothiophene-based conjugated liquid crystal and its implication for ionic conductivity characteristics. *Adv. Funct. Mater.* **29**, 1805220 (2019).
27. B. X. Dong, Z. Liu, M. Misra, J. Strzalka, J. Niklas, O. G. Poluektov, F. A. Escobedo, C. K. Ober, P. F. Nealey, S. N. Patel, Structure control of a π-conjugated oligothiophene-based liquid crystal for enhanced mixed ion/electron transport characteristics. *ACS Nano* **13**, 7665–7675 (2019).
28. Z. Wang, C. Wang, Y. Sun, K. Wang, J. W. Strzalka, S. N. Patel, P. F. Nealey, C. K. Ober, F. A. Escobedo, Ion transport in 2D nanostructured π-conjugated thieno[3,2-*b*] thiophene-based liquid crystal. *ACS Nano* **16**, 20714–20729 (2022).
29. W. H. Meyer, Polymer electrolytes for lithium-ion batteries. *Adv. Mater.* **10**, 439–448 (1998).
30. H. Wu, C. D. Wick, Computational investigation on the role of plasticizers on ion conductivity in poly(ethylene oxide) LiTFSI electrolytes. *Macromolecules* **43**, 3502–3510 (2010).
31. O. Borodin, G. D. Smith, Mechanism of ion transport in amorphous poly(ethylene oxide)/litfsi from molecular dynamics simulations. *Macromolecules* **39**, 1620–1629 (2006).
32. M. Funahashi, J. Hanna, High ambipolar carrier mobility in self-organizing terthiophene derivative. *Appl. Phys. Lett.* **76**, 2574–2576 (2000).
33. K. L. Woon, M. P. Aldred, P. Vlachos, G. H. Mehl, T. Stirner, S. M. Kelly, M. O'Neill, Electronic charge transport in extended nematic liquid crystals. *Chem. Mater.* **18**, 2311–2317 (2006).
34. S. Yazaki, M. Funahashi, T. Kato, An electrochromic nanostructured liquid crystal consisting of π-conjugated and ionic moieties. *J. Am. Chem. Soc.* **130**, 13206–13207 (2008).
35. V. Percec, M. Glodde, T. K. Bera, Y. Miura, I. Shiyanovskaya, K. D. Singer, V. S. K. Balagurusamy, P. A. Heiney, I. Schnell, A. Rapp, H. W. Spiess, S. D. Hudson, H. Duan, Self-organization of supramolecular helical dendrimers into complex electronic materials. *Nature* **419**, 384–387 (2002).
36. T. Yasuda, T. Shimizu, F. Liu, G. Ungar, T. Kato, Electro-functional octupolar π-conjugated columnar liquid crystals. *J. Am. Chem. Soc.* **133**, 13437–13444 (2011).
37. T. Ichikawa, M. Yoshio, A. Hamasaki, T. Mukai, H. Ohno, T. Kato, Self-organization of room-temperature ionic liquids exhibiting liquid-crystalline bicontinuous cubic phases: Formation of nano-ion channel networks. *J. Am. Chem. Soc.* **129**, 10662–10663 (2007).
38. T. Ichikawa, M. Yoshio, A. Hamasaki, S. Taguchi, F. Liu, X. Zeng, G. Ungar, H. Ohno, T. Kato, Induction of thermotropic bicontinuous cubic phases in liquid-crystalline ammonium and phosphonium salts. *J. Am. Chem. Soc.* **134**, 2634–2643 (2012).
39. T. Kato, N. Mizoshita, K. Kishimoto, Functional liquid-crystalline assemblies: Self-organized soft materials. *Angew. Chem. Int. Ed. Engl.* **45**, 38–68 (2006).
40. C. Tschierske, Development of structural complexity by liquid-crystal self-assembly. *Angew. Chem. Int. Ed. Engl.* **52**, 8828–8878 (2013).
41. Y. Sun, P. Padmanabhan, M. Misra, F. A. Escobedo, Molecular dynamics simulation of thermotropic bolaamphiphiles with a swallow-tail lateral chain: Formation of cubic network phases. *Soft Matter* **13**, 8542–8555 (2017).
42. Y. Sun, F. A. Escobedo, Coarse-grained molecular simulation of bolapolyphiles with a multident lateral chain: Formation and structural analysis of cubic network phases. *J. Chem. Theory Comput.* **20**, 1519–1537 (2024).
43. Z. Xue, D. He, X. Xie, Poly(ethylene oxide)-based electrolytes for lithium-ion batteries. *J. Mater. Chem. A* **3**, 19218–19253 (2015).
44. M. Misra, Z. Liu, B. X. Dong, S. N. Patel, P. F. Nealey, C. K. Ober, F. A. Escobedo, Thermal stability of π-conjugated n-ethylene-glycol-terminated quaterthiophene oligomers: A computational and experimental study. *ACS Macro Lett.* **9**, 295–300 (2020).
45. P. K. Lo, D. Chen, Q. Meng, M. S. Wong, Highly ordered smectic phases from polar calix[4] arene derivatives. *Chem. Mater.* **18**, 3924–3930 (2006).
46. W. Chen, B. Wunderlich, Nanophase separation of small and large molecules. *Macromol. Chem. Phys.* **200**, 283–311 (1999).
47. D. K. Paul, R. McCreery, K. Karan, Proton transport property in supported nafion nanothin films by electrochemical impedance spectroscopy. *J. Electrochem. Soc.* **161**, F1395–F1402 (2014).
48. C. G. Arges, Y. Kambe, H. S. Suh, L. E. Ocola, P. F. Nealey, Perpendicularly aligned, anion conducting nanochannels in block copolymer electrolyte films. *Chem. Mater.* **28**, 1377–1389 (2016).
49. H. Shimura, M. Yoshio, A. Hamasaki, T. Mukai, H. Ohno, T. Kato, Electric-field-responsive lithium-ion conductors of propylenecarbonate-based columnar liquid crystals. *Adv. Mater.* **21**, 1591–1594 (2009).
50. A. Eisele, K. Kyriakos, R. Bhandary, M. Schönhoff, C. M. Papadakis, B. Rieger, Structure and ionic conductivity of liquid crystals having propylene carbonate units. *J. Mater. Chem. A* **3**, 2942–2953 (2015).
51. D. Deng, M. A. Webb, P. Bennington, D. Sharon, P. F. Nealey, S. N. Patel, J. J. de Pablo, Role of molecular architecture on ion transport in ethylene oxide-based polymer electrolytes. *Macromolecules* **54**, 2266–2276 (2021).

52. B. X. Dong, C. Nowak, J. W. Onorato, J. Strzalka, F. A. Escobedo, C. K. Luscombe, P. F. Nealey, S. N. Patel, Influence of side-chain chemistry on structure and ionic conduction characteristics of polythiophene derivatives: A computational and experimental study. *Chem. Mater.* **31**, 1418–1429 (2019).
53. W. Chu, M. A. Webb, C. Deng, Y. J. Colón, Y. Kambe, S. Krishnan, P. F. Nealey, J. J. de Pablo, Understanding ion mobility in P2VP/NMP$^{+}$I$^{-}$ polymer electrolytes: A combined simulation and experimental study. *Macromolecules* **53**, 2783–2792 (2020).
54. M. A. Webb, U. Yamamoto, B. M. Savoie, Z. G. Wang, T. F. Miller III, Globally suppressed dynamics in ion-doped polymers. *ACS Macro Lett.* **7**, 734–738 (2018).
55. M. A. Webb, Y. Jung, D. M. Pesko, B. M. Savoie, U. Yamamoto, G. W. Coates, N. P. Balsara, Z. G. Wang, T. F. Miller III, Systematic computational and experimental investigation of lithium-ion transport mechanisms in polyester-based polymer electrolytes. *ACS Cent. Sci.* **1**, 198–205 (2015).
56. M. A. Webb, B. M. Savoie, Z. G. Wang, T. F. Miller III, Chemically specific dynamic bond percolation model for ion transport in polymer electrolytes. *Macromolecules* **48**, 7346–7358 (2015).
57. D. M. Pesko, M. A. Webb, Y. Jung, Q. Zheng, T. F. Miller III, G. W. Coates, N. P. Balsara, Universal relationship between conductivity and solvation-site connectivity in ether-based polymer electrolytes. *Macromolecules* **49**, 5244–5255 (2016).
58. S. Yan, Y. Lu, F. Liu, Y. Xia, Q. Li, K. Liu, Zwitterionic matrix with highly delocalized anionic structure as an efficient lithium ion conductor. *CCS Chem.* **5**, 1612–1622 (2023).
59. W. L. Jorgensen, D. S. Maxwell, J. Tirado-Rives, Development and testing of the OPLS all-atom force field on conformational energetics and properties of organic liquids. *J. Am. Chem. Soc.* **118**, 11225–11236 (1996).
60. S. Plimpton, Fast parallel algorithms for short-range molecular dynamics. *J. Comput. Phys.* **117**, 1–19 (1995).
61. A. P. Thompson, H. M. Aktulga, R. Berger, D. S. Bolintineanu, W. M. Brown, P. S. Crozier, P. J. In't Veld, A. Kohlmeyer, S. G. Moore, T. D. Nguyen, R. Shan, M. J. Stevens, J. Tranchida, C. Trott, S. J. Plimpton, LAMMPS - A flexible simulation tool for particle-based materials modeling at the atomic, meso, and continuum scales. *Comp. Phys. Commun.* **271**, 10817 (2022).
62. W. M. Brown, P. Wang, S. J. Plimpton, A. N. Tharrington, Implementing molecular dynamics on hybrid high performance computers – short range forces. *Comput. Phys. Commun.* **182**, 898–911 (2011).
63. W. M. Brown, A. Kohlmeyer, S. J. Plimpton, A. N. Tharrington, Implementing molecular dynamics on hybrid high performance computers – Particle–particle particle-mesh. *Comput. Phys. Commun.* **183**, 449–459 (2012).
64. W. Humphrey, A. Dalke, K. Schulten, VMD: Visual molecular dynamics. *J. Mol. Graphics* **14**, 33–38 (1996).
65. D. Sharon, P. Bennington, C. Liu, Y. Kambe, B. X. Dong, V. X. Burnett, M. Dolejsi, G. Grocke, S. N. Patel, P. F. Nealey, Interrogation of electrochemical properties of polymer electrolyte thin films with interdigitated electrodes. *J. Electrochem. Soc.* **165**, H1028–H1039 (2018).
66. Z. Jiang, GIXSGUI: A MATLAB toolbox for grazing-incidence X-ray scattering data visualization and reduction, and indexing of buried three-dimensional periodic nanostructured films. *J. Appl. Cryst.* **48**, 917–926 (2015).
67. B. X. Dong, J. Strzalka, Z. Jiang, H. Li, G. E. Stein, P. F. Green, Crystallization mechanism and charge carrier transport in MAPLE-deposited conjugated polymer thin films. *ACS Appl. Mater. Interfaces* **9**, 44799–44810 (2017).
68. Y. Sun, "Computational study of self-assembly of amphiphilic and polyphilic molecules and application in li-ion transport," thesis, Cornell University, Ithaca, NY (2023).
69. H. S. Marsh, E. Jankowski, A. Jayaraman, Controlling the morphology of model conjugated thiophene oligomers through alkyl side chain length, placement, and interactions. *Macromolecules* **47**, 2736–2747 (2014).
70. H. Lee, A. H. de Vries, S. J. Marrink, R. W. Pastor, A coarse-grained model for polyethylene oxide and polyethylene glycol: Conformation and hydrodynamics. *J. Phys. Chem. B* **113**, 13186–13194 (2009).
71. Q. Du, Z. Yang, N. Yang, X. Yang, Coarse-grained model for perfluorocarbons and phase equilibrium simulation of perfluorocarbons/$CO_2$ mixtures. *Ind. Eng. Chem. Res.* **49**, 8271–8278 (2010).
72. P. Virnau, M. Müller, L. G. MacDowell, K. Binder, Phase behavior of *n*-alkanes in supercritical solution: A Monte Carlo study. *J. Chem. Phys.* **121**, 2169–2179 (2004).
73. F. A. Escobedo, Z. Chen, Liquid crystalline behavior of a semifluorinated oligomer. *J. Chem. Phys.* **121**, 11463–11473 (2004).
74. A. J. Rzepiela, L. V. Schäfer, N. Goga, H. J. Risselada, A. H. De Vries, S. J. Marrink, Reconstruction of atomistic details from coarse-grained structures. *J. Comput. Chem.* **31**, 1333–1343 (2010).
75. T. A. Wassenaar, K. Pluhackova, R. A. Böckmann, S. J. Marrink, D. P. Tieleman, Going backward: A flexible geometric approach to reverse transformation from coarse grained to atomistic models. *J. Chem. Theory Comput.* **10**, 676–690 (2014).
76. L. E. Lombardi, M. A. Martí, L. Capece, CG2AA: Backmapping protein coarse-grained structures. *Bioinformatics* **32**, 1235–1237 (2016).
77. J. Krajniak, S. Pandiyan, E. Nies, G. Samaey, Generic adaptive resolution method for reverse mapping of polymers from coarse-grained to atomistic descriptions. *J. Chem. Theory Comput.* **12**, 5549–5562 (2016).
78. J. Peng, C. Yuan, R. Ma, Z. Zhang, Backmapping from multiresolution coarse-grained models to atomic structures of large biomolecules by restrained molecular dynamics simulations using bayesian inference. *J. Chem. Theory Comput.* **15**, 3344–3353 (2019).
79. W. Li, C. Burkhart, P. Polińska, V. Harmandaris, M. Doxastakis, Backmapping coarse-grained macromolecules: An efficient and versatile machine learning approach. *J. Chem. Phys.* **153**, 041101 (2020).
80. B. S. John, C. Juhlin, F. A. Escobedo, Phase behavior of colloidal hard perfect tetragonal parallelepipeds. *J. Chem. Phys.* **128**, 044909 (2008).
81. P. Bennington, C. Deng, D. Sharon, M. A. Webb, J. J. de Pablo, P. F. Nealey, S. N. Patel, Role of solvation site segmental dynamics on ion transport in ethylene-oxide based side-chain polymer electrolytes. *J. Mater. Chem. A* **9**, 9937–9951 (2021).



**Acknowledgments**

**Funding:** We acknowledge financial support for this work through Designing Materials to Revolutionize and Engineer our Future (DMREF) grant from the National Science Foundation under contract no. DMREF-1922259. This work made use of the Cornell Center for Materials Research Shared Facilities which are supported through the NSF MRSEC program (DMR-1719875). The research also used the resources of the Advanced Photon Source, an Office of Science User Facility operated for the US Department of Energy (DOE) by Argonne National Laboratory under contract no. DE-AC02-06CH11357. **Author contributions:** Z.L. conducted materials synthesis and characterization on their thermal and optical properties. B.X.D. implemented GIWAX/WAXS and ionic conductivity measurements. Y.S. completed MD simulation on molecular packing and Li-ion solvation. Z.L., Y.S., and B.X.D. drafted the manuscript, with revisions from C.K.O., F.A.E., S.N.P., and P.F.N. All authors approved the final version of the manuscript. **Competing interests:** The authors declare that they have no competing interests. **Data and materials availability:** All data needed to evaluate the conclusions in the paper are present in the paper and/or the Supplementary Materials.

Submitted 21 October 2024
Accepted 11 April 2025
Published 16 May 2025
10.1126/sciadv.adt8303